



Electron transfer route tuning caused by photo-irradiation: Stability enhancement of N-doped carbon materials in Fenton-like reactions

Xiaomei Liu^a, Jun Wang^a, Tao Liao^a, Yang Li^{a,b}, Xiaobin Fan^{a,b}, Fengbao Zhang^a, Wenchao Peng^{a,b,*}

^a School of Chemical Engineering and Technology, Tianjin University, Tianjin 300350, China

^b Zhejiang Institute of Tianjin University, Shaoxing, Zhejiang 312300, China

ARTICLE INFO

Keywords:

N-doped carbon materials
Photo-irradiation
Electrons transport route
DET process
Stability

ABSTRACT

Improving the stability of N-doped carbon materials is still a great challenge in Fenton-like reactions. Herein, a hollow structure with TiO₂ nanoparticles supported on the inner surface of N-doped carbon spheres (H-TiO₂@NC) is designed for peroxydisulfate (PDS)-based Fenton-like reactions with photo-irradiation. Impressively, the stability of H-TiO₂@NC is greatly enhanced with photo-irradiation. The degradation rate constant of bisphenol A (BPA) with photo-irradiation is ~61 times larger than dark condition after four runs. The photovoltage enables more electrons to be transferred from BPA to PDS via active carbons. Less electrons from the carbon framework are expended, thus inhibiting the oxidation and deactivation of H-TiO₂@NC effectively. Additionally, the direct electron transfer (DET) process is improved due to conductivity enhancement, which also weakens the oxidation of carbon skeleton. This work provides a reliable method to enhance the stability of N-doped carbon materials. And giving some new insights into the mechanism of stability enhancement.

1. Introduction

In recent years, N-doped carbon materials have been widely used in persulfates-based advanced oxidation processes (AOPs) on account of their low cost, nontoxic and high efficiency for pollutants degradation. Generally, the doping types of nitrogen in carbon framework include graphitic, pyridinic and pyrrolic nitrogen, in which graphitic nitrogen is considered as the main active site for persulfates activation [1–3]. When persulfates adsorb on graphitic nitrogen atoms, the electrons of carbon atoms around graphitic nitrogen can be abstracted by persulfates, resulting in the efficient activation of persulfates. Wang et al. [2,4–6] and Peng et al. [7–10] have synthesized many N-doped carbon materials as highly efficient catalysts for persulfates activation.

Although N-doped carbon materials show high efficiency for persulfates activation, their stabilities are still unsatisfactory [5,7,8,11]. For instance, Peng and co-workers synthesized nitrogen and sulfur co-doped graphene materials (N, S-G) by porous engineering and doping strategies. This material showed excellent phenol degradation performance with peroxymonosulfates (PMS) as oxidant and the corresponding reaction rate constant (*k*) is 0.368 min^{−1} [7]. Additionally, hierarchically nitrogen-doped porous carbons were also prepared via a one-pot

pyrolysis process, which exhibited outstanding catalytic performance for phenol removal with a very high *k* value of 1.300 min^{−1} [8]. However, during durability tests, the *k* values drop fast after the first run. One of the deactivation reasons of N-doped carbon materials is that the carbon atoms are continuously oxidized by persulfates, which results in the generation of abundant oxygen-containing functional groups (OFGs) on the carbon skeleton [12]. Till now, high temperature thermal treatment is often employed to remove OFGs to prolong the lifetime of N-doped carbon materials, which is difficult and will need large amounts of energy [13–15]. Therefore, it's still a great challenge to improve the antioxidation of N-doped carbon materials to maintain their long-term stabilities. In our previous studies, the photoelectrons generated by g-C₃N₄ can inhibit the oxidation of cobalt metals, thereby accelerating the in situ regeneration of highly reactive low-valent metal ions (Co²⁺) for peroxydisulfates (PDS) activation [16]. Inspired by this, we wonder whether the antioxidation of N-doped carbon materials can be improved by the introduction of photo-irradiation assistant during persulfates-based AOPs. To date, although many photocatalytic composites have demonstrated excellent stability for pollutants degradation under photo-irradiation, the specific mechanism of their outstanding stability has not been deeply investigated [17–20].

* Corresponding author at: School of Chemical Engineering and Technology, Tianjin University, Tianjin 300350, China.

E-mail address: wenchao.peng@tju.edu.cn (W. Peng).

<https://doi.org/10.1016/j.apcatb.2023.123261>

Received 13 June 2023; Received in revised form 12 August 2023; Accepted 2 September 2023

Available online 4 September 2023

0926-3373/© 2023 Elsevier B.V. All rights reserved.

As one of the nonradical activation pathways of persulfates, the direct electron transfer (DET) process often occurs on N-doped carbon materials [5,21,22]. In DET process, persulfates can directly abstract electrons from the co-adsorbed pollutants on the surface of N-doped carbon materials, resulting in the reduction of persulfates into sulfate ions rather than cleaving the O-O bond into free radicals [14,23]. For the radical activation of persulfates, N-doped carbon materials can be continuously oxidized by persulfates. However, during DET process, N-doped carbon materials act as electron transport conductors cannot be oxidized by persulfates. Therefore, improving the contribution of DET process is conducive to enhance the antioxidation of N-doped carbon materials. Good conductivity is beneficial for electrons transfer, which plays an important role for DET process enhancement. It's reported that photo-irradiation can excite photocatalytic semiconductors to produces numerous microdevices with photovoltage, which can enhance the conductivity of composites greatly [24–26]. Thus, designing and synthesizing reasonable structures for N-doped carbon materials and semiconductors is expected to inhibit the oxidation of N-doped carbon materials in Fenton-like reactions.

In this study, SiO_2 was firstly wrapped by TiO_2 nanoparticles, which was then used as template for the deposition of N-doped carbon (NC) layers via a chemical vapor deposition (CVD) method. After the etching of SiO_2 , the H-TiO_2 @NC with hollow structure was obtained. The activities and stabilities of H-TiO_2 @NC under light and dark conditions are evaluated respectively with PDS as oxidant and BPA as model pollutant. Combined with DFT calculations, the antioxidation mechanism of H-TiO_2 @NC under light irradiation was established. Additionally, under light irradiation, the activation mechanism of PDS on H-TiO_2 @NC was determined by quenching experiments, electron paramagnetic resonance (EPR), open circuit potential (OCP), and in situ Raman tests. Finally, the interference resistance of water body and universality of H-TiO_2 @NC/PDS/light system were also investigated.

2. Experimental section

2.1. Synthesis of SiO_2 @ TiO_2

The SiO_2 @ TiO_2 was prepared according to a previous report [27]. 1.0 g of as-prepared SiO_2 nanoparticles was added into a mixture containing 79 mL of ethanol, 3.9 mL of ammonia solution, and 1.4 mL of water to form SiO_2 colloidal solution. Subsequently, 28 mL of acetonitrile was added into the SiO_2 colloidal solution with stirring at 4 °C (solution A). Solution B containing 36 mL of ethanol, 12 mL of acetonitrile, and 1 mL of titanium isopropoxide was added dropwise into solution A. Then, the above mixture was stirred vigorously for 12 h, and the resulting solution was dried at 80 °C. Finally, after calcining at 600 °C for 6 h, the white powder of SiO_2 @ TiO_2 was obtained.

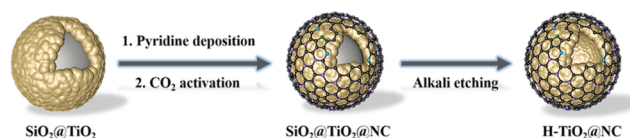
2.2. Synthesis of H-TiO_2 @NC

H-TiO_2 @NC was prepared by a CVD method. Typically, a quartz boat with SiO_2 @ TiO_2 template was placed in the quartz tube furnace of a CVD system. When the furnace was heated to 900 °C with a heating rate of 30 °C min⁻¹, gaseous pyridine, which was evaporated by bubbling liquid pyridine with an Ar flow (100 sccm), flowed through the tubular quartz reactor for 10 min. Subsequently, CO_2 (100 sccm) was switched into the CVD system and maintained for 20 min. After cooling down naturally, the SiO_2 @ TiO_2 @NC was obtained. H-TiO_2 @NC was synthesized by etching SiO_2 @ TiO_2 @NC in 1 M NaOH solution at 90 °C for 3 h.

3. Results and discussion

3.1. Structural characterization of H-TiO_2 @NC

As shown in Scheme 1, hollow sphere H-TiO_2 @NC was synthesized



Scheme 1. Illustration of the synthesis process for H-TiO_2 @NC.

by a CVD method and the subsequent alkali etching process. The TiO_2 nanoparticles were firstly coated onto the SiO_2 template by a sol-gel method (Figs. S1a and b) [27]. During the following CVD process, pyridine was carbonized and evenly deposited on the surface of core-shell SiO_2 @ TiO_2 to form N-doped carbon layers (Fig. S1c). Then, CO_2 was employed to activate the NC layers. Finally, the SiO_2 template was etched by NaOH solution to produce a hollow N-doped carbon sphere structure with TiO_2 supported on the inner surface (H-TiO_2 @NC).

To investigate the detailed structure of H-TiO_2 @NC, the SEM, TEM images, XRD pattern, Raman, and FTIR spectra are depicted in Fig. 1. As shown in Fig. 1a and b, H-TiO_2 @NC displays a hollow sphere structure. The hollow spherical structure of H-TiO_2 @NC not only enhances the specific surface area but also improves the light utilization efficiency [28,29]. The HRTEM images of H-TiO_2 @NC reveal that TiO_2 has two phases of anatase (101) and rutile (110) (Fig. 1c and S2). The co-existence of anatase and rutile is conducive to reduce the recombination probability of photogenerated electron-hole pairs [30,31]. Additionally, the TiO_2 nanoparticles with different sizes are obviously wrapped by NC layers with a thickness of ~2 nm. It should be noted that the thickness of NC layers is ~7 nm without CO_2 activation (Fig. S3a). Thus, CO_2 activation here decreased the thickness of NC layers rather than digging pores on NC layers (Figs. S3b and c) [7,32]. No individual NC flakes can be observed on the surface of TiO_2 , implying NC layers contact intimately with TiO_2 nanoparticles. The EDS mapping images and line-scan spectra of H-TiO_2 @NC show a distinct elemental distribution characteristic of hollow sphere (Fig. 1d1-d5 and S4). Moreover, the uneven distribution of elements might be ascribed to the shedding of TiO_2 nanoparticles during alkali etching process and the interconnected gaps existed between TiO_2 nanoparticles. H-TiO_2 @NC shows a hollow sphere structure with two surfaces. The inner surface is composed of TiO_2 nanoparticles of different sizes, and the outer shell is NC layers. In Fig. 1e, the XRD pattern shows several obvious diffraction peaks at 25.3°, 37.7°, 48.1°, 55.1° and 62.7° corresponding to the (101), (004), (200), (211) and (204) facets of anatase-phase TiO_2 (PDF#71-1166), respectively. Meanwhile, the characteristic peaks at 27.4°, 36.1°, 41.2°, 44.0°, 54.3°, 56.6° and 64.0° are observed, which are indexed to the (110), (101), (111), (210), (211), (220) and (310) facets of rutile-phase TiO_2 (PDF#75-1748), respectively [31]. The XRD results are consistent well with HRTEM. The XRD pattern of SiO_2 @ TiO_2 is shown in Fig. S5, no characteristic peaks related to rutile TiO_2 can be observed. Therefore, the rutile TiO_2 should be transformed from anatase TiO_2 gradually during the CVD process. According to the Spurr-Myers formula, the mass percentage of anatase-phase TiO_2 is ~41% [33]. The Raman spectra of H-TiO_2 @NC are depicted in Fig. 1f, the characteristic peaks at ~147 cm⁻¹ and 634 cm⁻¹ are attributed to E_g (symmetric O-Ti-O stretching). And the characteristic peaks at ~396 cm⁻¹ and 519 cm⁻¹ are assigned to B_{1g} (symmetric O-Ti-O bending) and A_{1g} (antisymmetric O-Ti-O bending), respectively [34]. Two distinct peaks at ~1353 and 1593 cm⁻¹ correspond to the D band of defective carbon peak and G band of crystalline graphitic carbon peak respectively, further confirming the successful deposition of NC layers [7,35]. The FT-IR spectra are shown in Fig. 1g, the typical peaks at ~3437 cm⁻¹, 2922 cm⁻¹, 1626 cm⁻¹, 1382 cm⁻¹ and 1107 cm⁻¹ are attributed to the stretching vibrations of O-H, C-H, C=O, aromatic C=C and C-O, respectively [36]. Another broad band at ~400–700 cm⁻¹ belongs to the Ti-O stretching vibration. Additionally, no obvious peaks related to C-N bonds can be observed due to the relatively low doping content of nitrogen.

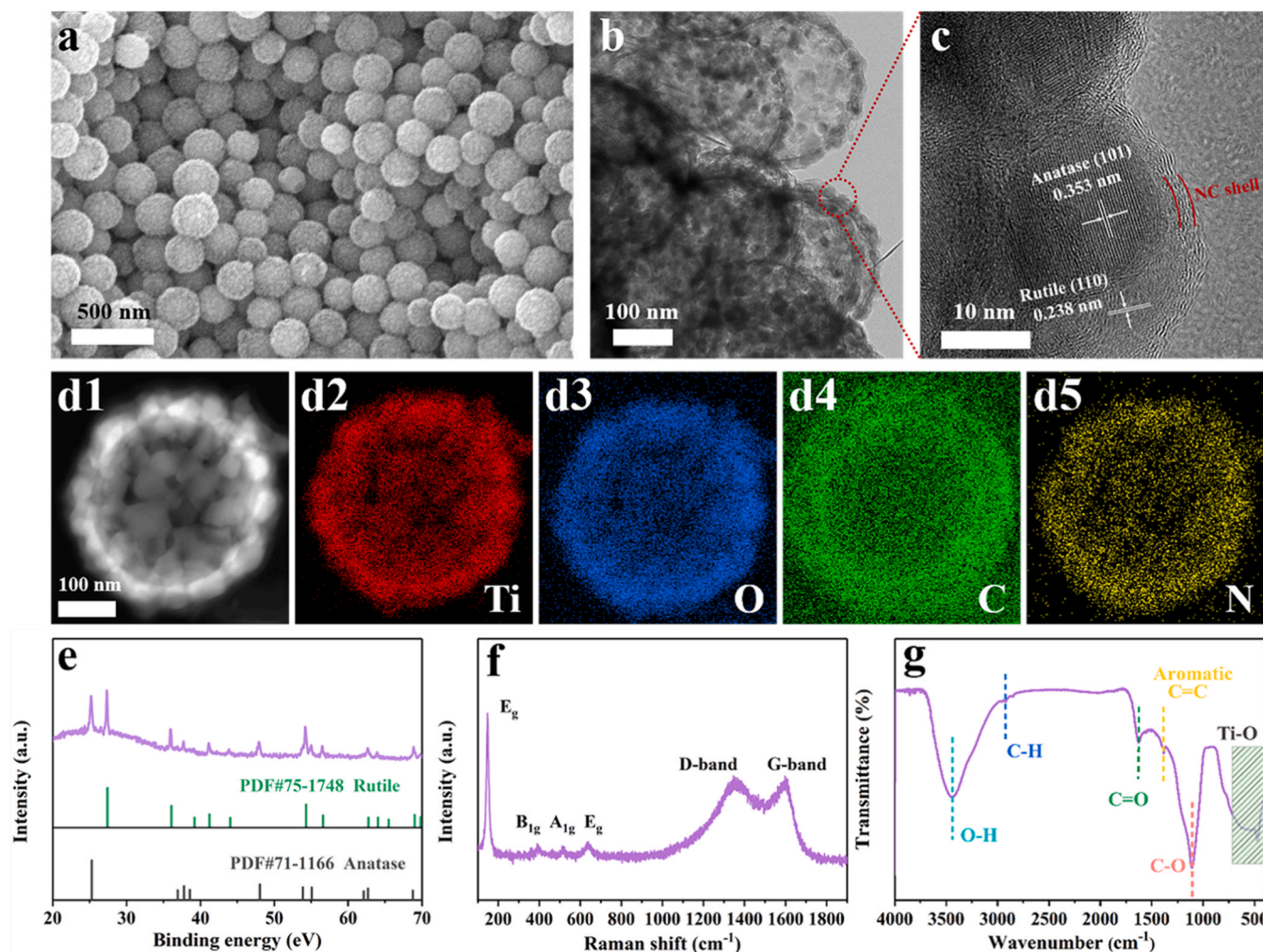


Fig. 1. Morphological and structural characterization of H-TiO₂ @NC. (a) SEM, (b) TEM, (c) HRTEM, and (d1-d5) EDS mapping images. (e) XRD, (f) Raman spectra, and (g) FTIR spectra.

3.2. Performance evaluation

The catalytic activities and stabilities of H-TiO₂ @NC were investigated. Before photocatalytic reaction, an adsorption treatment under dark was performed to reach the adsorption-desorption equilibrium. The adsorption of BPA by H-TiO₂ @NC is negligible (Fig. S6a). As shown in Fig. 2a, catalyst cannot be activated to degrade BPA by light directly without PDS. Moreover, BPA cannot be degraded by H-TiO₂ @NC only via photocatalysis process without PDS. However, H-TiO₂ @NC can activate PDS to degrade ~80% BPA within 40 min under dark condition, and the reaction rate constant (k) value was calculated to be 0.037 min⁻¹. Under light irradiation, it can degrade ~100% of BPA within 40 min with a k value of 0.126 min⁻¹, which is ~3.4 times larger than that without light. Additionally, only ~32% of BPA can be removed within 40 min in H-TiO₂/PDS/light system, indicating that PDS cannot be activated effectively by H-TiO₂ without NC layers even under light irradiation (Fig. S6b). For H-TiO₂/PDS/dark system, the degradation of BPA is negligible, which suggests that H-TiO₂ had no chemical activity for PDS activation.

The stabilities of H-TiO₂ @NC with or without light irradiation are also tested and shown in Fig. 2b. Under light irradiation, ~85% of BPA can still be removed even after five runs, surpassing most of the reported N-doped carbon-based materials (Table S2). However, under dark condition, BPA can hardly be degraded only after the first run. Moreover, the k_{light} in the light system can maintain a high value for a long time, while the k_{dark} from the first run to the second run decreases sharply

under dark condition (Fig. 2c). Obviously, the k/k_0 value is higher under light irradiation and its decline rate is much slower than in dark condition (Fig. 2d). It's speculated that the photovoltage generated by H-TiO₂ under light irradiation can affect the electron distribution of NC layers, which might further influence the activity and stability of H-TiO₂ @NC for PDS activation. In Fig. S7, the H-TiO₂ @NC was firstly used for one cycle under light irradiation, which was then used for the degradation process without light. The k value of this dark process is 0.035 min⁻¹, which is comparable to the fresh H-TiO₂ @NC under dark condition (0.037 min⁻¹). However, the k value decreases sharply from 0.035 min⁻¹ to 0.005 min⁻¹ in the second cycle. Therefore, it can be concluded that the catalytic activity and stability of H-TiO₂ @NC for PDS activation under light irradiation are superior to that under dark condition.

3.3. Mechanism analysis of stability enhancement

Based on the above results, it's found that the light irradiation can affect the stabilities of H-TiO₂ @NC for PDS activation greatly. The excessive oxygen-containing functional groups (OFGs) on the surface of carbonaceous materials not only deteriorate the conductivity but also reduce the exposure of active sites. It seriously affects the activation performance of carbon-based materials for PDS [14,37]. Therefore, the XPS spectra of H-TiO₂ @NC after each stability run were analyzed. As shown in Fig. S8, the broad O 1s peak can be deconvoluted into five peaks at ~530.5 eV, 531.1 eV, 532.8 eV, 533.6 eV and 534.4 eV,

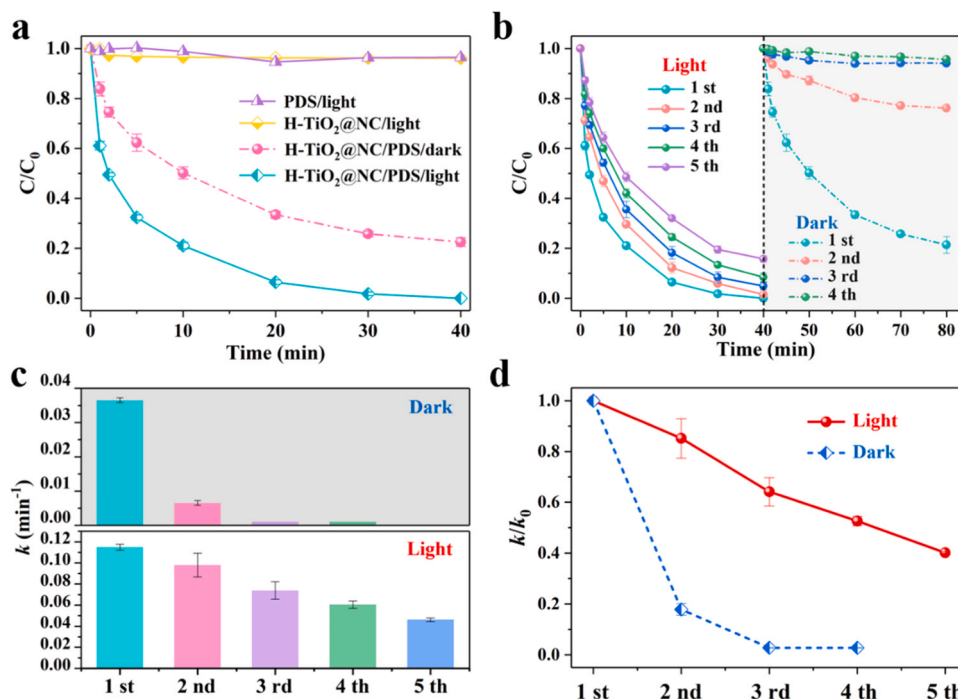


Fig. 2. (a) BPA degradation under different reaction systems. (b) Stability testing of H-TiO₂@NC. (c) The corresponding k values. (d) k/k_0 values of each run (k_0 is the reaction rate constant of the first run). Reaction conditions: [BPA]₀ = 20 mg/L, PDS = 0.25 g/L, [catalyst] = 0.1 g/L, under simulated sunlight.

corresponding to the lattice oxygen of TiO₂, carbonyl group (C=O), carboxyl group (O-C=O), hydroxyl group (C-OH) and adsorbed H₂O/O₂, respectively [34,36,38]. Fig. S9 depicts the Ti 2p and C 1s XPS spectra. The C 1s spectra have five carbon species at the binding energies of C-C/C-N (284.7 eV), C-O (285.5 eV), C=O (286.9 eV), and O-C=O (290.1 eV), which further verifies the types of OFGs. According

to the O 1s XPS spectra, the OFGs contents of H-TiO₂@NC are shown in Fig. 3a. The OFGs content of H-TiO₂@NC under dark condition increases faster than that under light irradiation. Significantly, under dark condition, the OFGs content increases sharply from the first run to the second run, which can also be reflected by the rapid decay of stability. In detail, under dark condition, C-OH and O-C=O content increases from

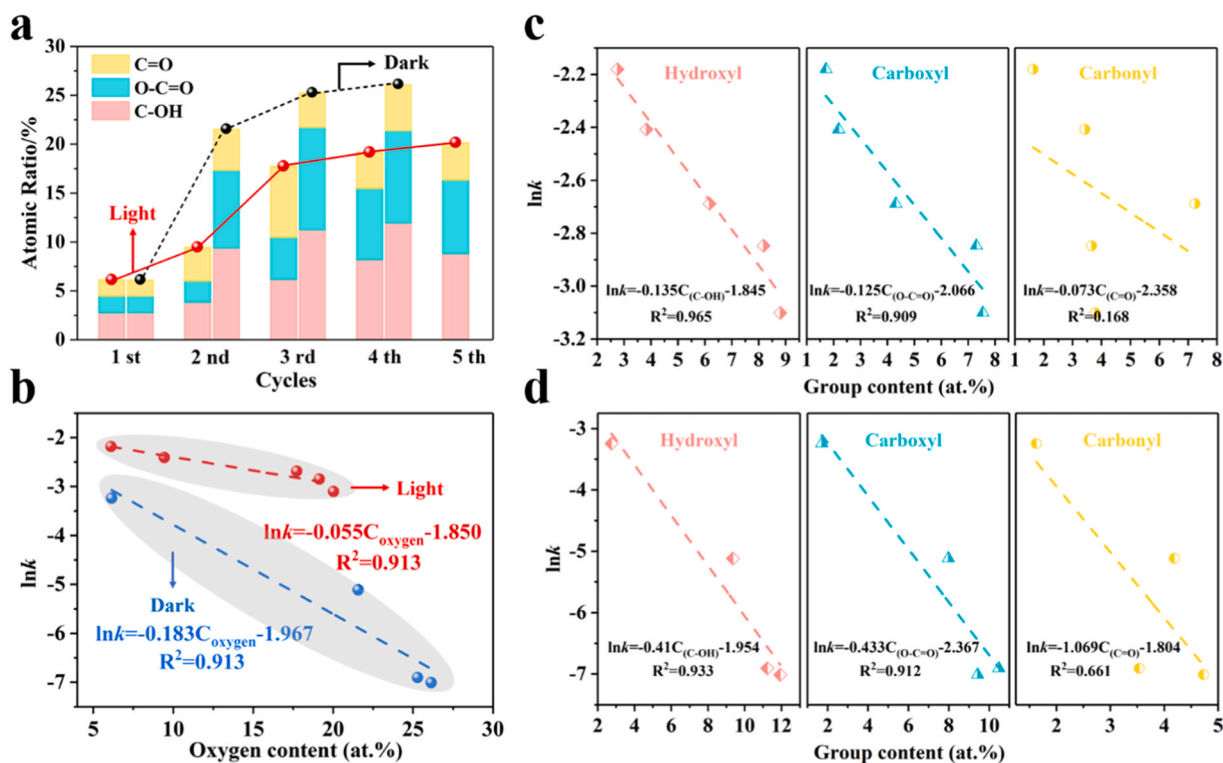


Fig. 3. (a) Atomic percentage of OFGs in H-TiO₂@NC under light and dark conditions. (b) Correlation of $\ln k$ to total OFGs content. Correlation of $\ln k$ to different OFGs contents in light (c) and dark (d) systems.

2.75% and 1.72% in the first run to 9.36% and 7.98% in the second run, respectively (Table S3). However, under light irradiation, C-OH and O-C=O content increases from 2.75% and 1.72% in the first run to 3.83% and 2.19% in the second run, respectively (Table S3). It can be observed that the increase rate of C-OH and O-C=O groups under light irradiation is much slower than that dark condition. The content of C=O changes irregularly with the increase of stability runs. These results demonstrate that the excessive C-OH and O-C=O groups might have an adverse effect on the stability of H-TiO₂@NC for PDS activation.

As shown in Fig. 3b, a well-fitted and negative linear relationship is observed between lnk and OFGs content under light (Eq. S3) and dark (Eq. S4) conditions, which suggests that the excessive OFGs indeed are not conducive to the long-term durability of H-TiO₂@NC. It's worth noting that the coefficient of Eq. (S4) is smaller than Eq. (S3), indicating that the faster increase rate of OFGs in dark system leads to the poorer stability. Fig. 3c and d depict that C-OH and O-C=O groups in light and dark systems show good and negative linear relationship with lnk (Eqs. S5 and S6, Eqs. S8 and S9), suggesting that C-OH and O-C=O groups increase is unfavorable for the durability of catalyst. Conversely, C=O group with relatively low R² exhibits negligible effect on the stability (Eqs. S7 and S10), which might be ascribed to the fact that C=O moieties can serve as the typical active sites for persulfate activation [6]. Additionally, the used H-TiO₂@NC in light and dark systems are then annealed at 800 °C. The catalytic activities of H-TiO₂@NC can be recovered effectively (Fig. S10a). After the thermal treatment, the oxygen content of used H-TiO₂@NC in light (27.99%) and dark systems (38.46%) decreases sharply to 8.98% and 15.03%, respectively (Fig. S10b and c). It implies that the high OFGs content indeed is the main reason for the deactivation of H-TiO₂@NC catalyst.

The increase of OFGs content results in a decreased proportion of the doped nitrogen atoms. The doped nitrogen atoms in carbon-based materials are the typical active sites for persulfates activation, thus the N 1 s XPS spectra after each cycling are also analyzed (Fig. S11). Fig. S12a shows that the decline rate of nitrogen content under light irradiation is much slower than under dark condition. As shown in Fig. S12b, lnk presents a good and positive linear correlation with nitrogen content, suggesting that the doped nitrogen atoms are conducive to the catalytic activation of persulfates. Graphitic N shows the best linear relationship

with lnk, which indicates that graphitic N is the main active site for persulfates activation (Fig. S12c and d) [2,3,7]. During the stability testing, the content of graphitic N in light system is higher than that dark system, which further verifies the superior stability of H-TiO₂@NC.

It can be concluded that the increase rate of OFGs under dark condition is much faster than that under light irradiation. And C-OH and O-C=O groups increase is the main reason that leads to the deactivation of H-TiO₂@NC catalyst. A series of tests, including Zeta potential, OCP, Raman, and EIS are employed to verify the change of OFGs content during the stability cycling. After each stability run, Zeta potentials of H-TiO₂@NC are measured to explore the surface charge of H-TiO₂@NC with different level of OFGs. The increase of OFGs on the surface of carbon-based catalysts will decrease the Zeta potential [14]. As shown in Fig. 4a, the Zeta potential of H-TiO₂@NC under light irradiation declines from -8.20 mV to -21.51 mV after five runs, while the Zeta potential in dark system decreases rapidly to -40.06 mV after four runs (Table S4). An increase in the content of OFGs on H-TiO₂@NC will make the Zeta potential of H-TiO₂@NC become more negative, which hinders the adsorption of PDS due to stronger electrostatic repulsion [14,37]. The results of OCP tests are shown in Fig. 4b, the potential rises sharply with PDS addition and then gradually reaches an equilibrium value. The equilibrium value is identified as the potential of catalyst-PDS* complexes [28]. A stronger PDS adsorption ability of catalyst will improve the potential of catalyst-PDS* complexes. A larger potential of catalyst-PDS* complex indicates its stronger oxidative ability, which is favorable for the degradation of pollutants through DET process [21,23]. In Fig. 4b, under light irradiation, the potential of H-TiO₂@NC-PDS* decreases much slower than dark condition (Table S5). Notably, even after the fifth run, the potential of H-TiO₂@NC-PDS* in light system is still higher than that dark system. The slower decrease rate of potential contributes to the stability enhancement of H-TiO₂@NC.

It has been reported that the I_D/I_G value according to Raman test can be used to estimate the degree of structural disorder/defect of carbon-based materials [7,39]. The greater value of I_D/I_G implies that the more OFGs might be generated on the surface of carbonaceous materials. As depicted in Fig. 4c, the increasing rate of I_D/I_G value in dark system is faster than in light system (Table S6). Under light irradiation,

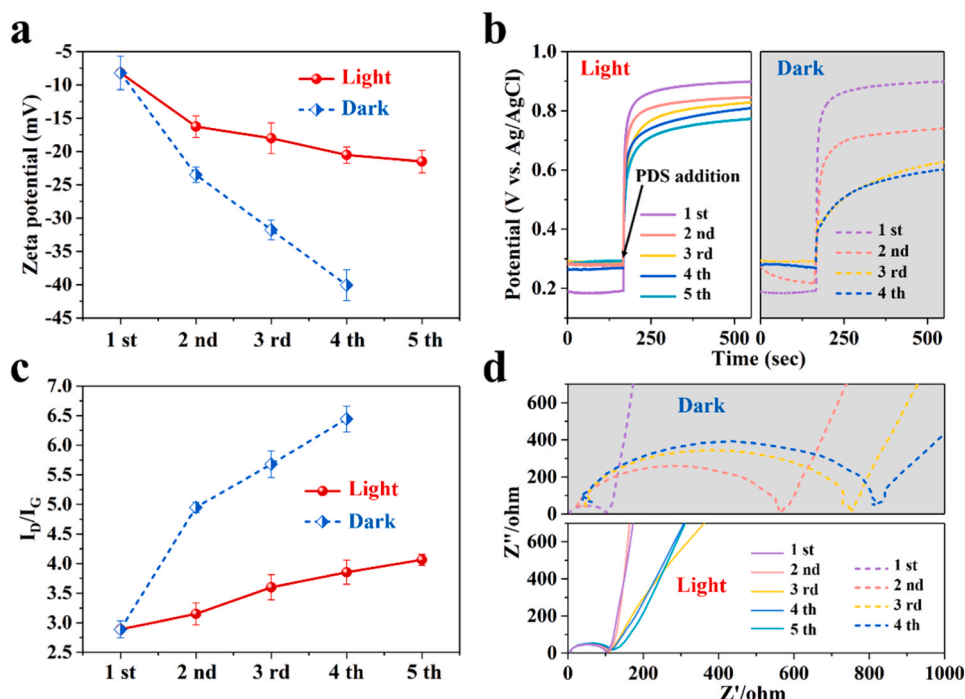


Fig. 4. Zeta potentials (a), OCP curves (b), I_D/I_G values according to Raman tests (c), and EIS tests (d) of H-TiO₂@NC in light and dark systems.

even after five runs, the I_D/I_G value of H-TiO₂@NC is still smaller than in dark condition. The conductivity of carbon-based materials can be greatly affected by the degree of structural disorder/defect [14]. As shown in Fig. 4d, the impedance of H-TiO₂@NC in light system is much smaller than dark system. Specifically, after the fourth run, the charge transfer resistance (R_{ct}) value of H-TiO₂@NC under dark condition is ~ 7.33 times larger than that light system (Table S7). It also indicates that the OFGs increase rate under light irradiation is much slower than dark condition. Compared with dark condition, the Zeta potential and H-TiO₂@NC-PDS* potential of H-TiO₂@NC are more positive, and the I_D/I_G value and impedance of H-TiO₂@NC are relatively small under light irradiation. It can be speculated that the photogenerated carriers can affect the electron distribution of NC layers wrapped on TiO₂ nanoparticles, which might influence the antioxidation and stability of H-TiO₂@NC.

The density functional theory (DFT) calculations were employed to verify the antioxidant mechanism of H-TiO₂@NC. Graphene-structured carbon-based materials with outstanding conductivity and electron mobility properties, such as graphene, carbon nanotubes, and graphene-like carbon-based materials, can be used as ideal electron sink or electron transfer media [40–42]. As shown in Fig. 5a, an obvious electron transport channel is observed between TiO₂ and NC layer (Fig. S13), and the number of electrons transferred from TiO₂ to NC layer is 0.559 e. The electron transport channel is favorable for the rapid transfer of

photoelectrons from TiO₂ to NC. Moreover, H-TiO₂@NC exhibits higher photocurrent response than H-TiO₂ (Fig. S14), indicating that the photoelectron transport route present between TiO₂ and NC, thus inhibiting the recombination of carriers greatly. In Fig. S15, the conductivity of H-TiO₂@NC is stronger than TiO₂, which agrees well with the EIS results (Fig. S16). Thus, the electron hybrid orbital of TiO₂ can be changed by NC layer introduction, which effectively enhances the conductivity of H-TiO₂@NC. According to the radical activation pathway of PDS ($\text{PDS} \rightarrow \text{S}_2\text{O}_8^{2-} \rightarrow \text{SO}_4^{\cdot-} \rightarrow \text{SO}_4^{2-}$), the Gibbs free energies for PDS activation on NC and H-TiO₂@NC are calculated respectively (Figs. S17 and S18). NC shows stronger PDS adsorption ability (-3.271 eV) than H-TiO₂@NC (-3.077 eV). However, the O-O bond length of adsorbed PDS on H-TiO₂@NC is longer than that of NC (Table S8). Moreover, compared to NC (2.355 eV), less energy is required for H-TiO₂@NC (2.227 eV) in $\text{S}_2\text{O}_8^{2-} \rightarrow \text{SO}_4^{\cdot-}$ reaction step (Fig. S18). Therefore, the synergistic interaction between TiO₂ and NC contributes to the rapid transfer of photoelectrons and the high efficiency activation of PDS.

The graphitic N shows stronger adsorption capacity for PDS than the carbon atoms around graphitic N (Fig. S19), which further confirms that graphitic N serves as active sites for PDS activation. As shown in Fig. 5b, the antioxidant mechanism of H-TiO₂@NC is proposed. In dark system, PDS adsorbed on graphitic N will gain electrons from carbon atoms surrounding graphitic N. Thus, the carbon skeleton is continuously oxidized by PDS during stability cycling, leading to a sharp increase in

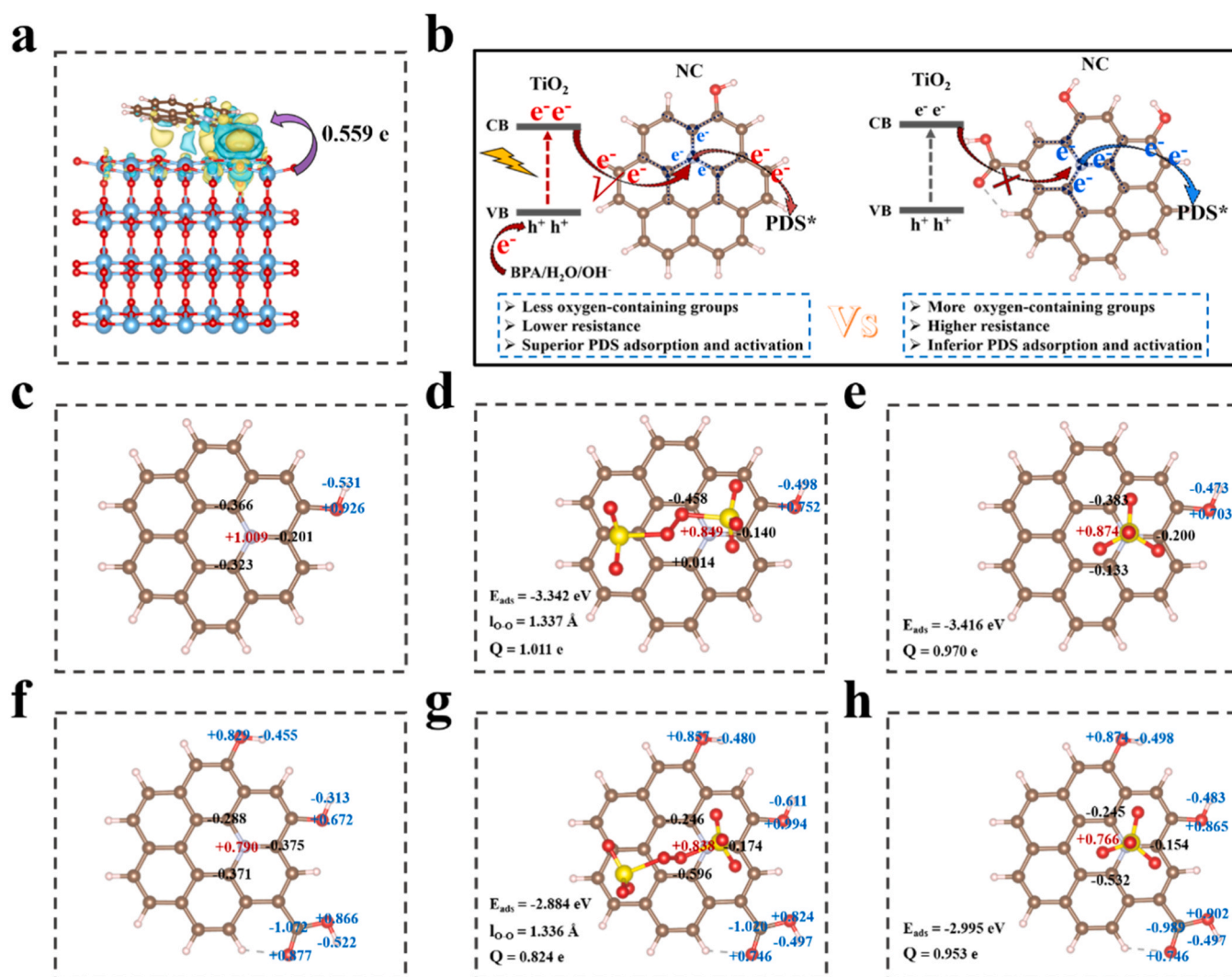


Fig. 5. (a) The charge density difference (CDD) of H-TiO₂@NC. (b) Schematic illustration of the antioxidant mechanism of H-TiO₂@NC. The calculated Bader charge of NC-OH (c), NC-OH adsorbed PDS (d), NC-OH adsorbed SO₄ (e), NC-OH/COOH (f), NC-OH/COOH adsorbed PDS (g), NC-OH/COOH adsorbed SO₄ (h).

OFGs [12]. A large number of OFGs can reduce the conductivity of H-TiO₂@NC, which greatly affects the electron transport process [14]. Moreover, abundant OFGs on the surface of catalysts will hinder the adsorption and activation of PDS due to steric hindrance effect and electrostatic repulsion [14,43]. Nevertheless, under light irradiation, PDS can obtain electrons via two pathways. Not only the carbon atoms surrounding graphitic N can provide electrons to PDS, but also the photoelectrons generated by TiO₂ can be rapidly transferred to PDS via electrons transport channel [44]. Importantly, the photogenerated holes with high valence band (VB) potential can react with BPA/H₂O/OH⁻ directly (Fig. S20), while this process will release electrons and transport onto the NC layers driven by photovoltage. This electrons transport route can thus slow down the electrons supply to PDS from carbon atoms. Therefore, the oxidation degree of H-TiO₂@NC is relatively lower under light irradiation than under dark condition. The electrons transport routes tuning for PDS activation might improve the

antioxidation of H-TiO₂@NC catalyst. After PDS pretreatment, the oxygen content of H-TiO₂@NC is higher under dark condition than light irradiation (Fig. S21), which corroborates the antioxidant mechanism of H-TiO₂@NC.

NC-OH containing less OFGs is constructed as the catalytic model of light system (Fig. 5c-e). Meanwhile, NC-OH/COOH with more OFGs is established as the catalytic model of dark system (Fig. 5f-h). In Fig. 5c and f, the Bader charge of graphitic N in NC-OH (+1.009) is higher than that in NC-OH/COOH (+0.790). It might be attributed to the fact that OH/COOH groups as electron-withdrawing groups can compete with graphitic N for electrons from carbon framework. Therefore, compared to NC-OH/COOH, NC-OH with fewer OFGs is more beneficial for PDS adsorption and activation. In Fig. 5d and g, NC-OH displays stronger PDS adsorption ability than NC-OH/COOH, indicating that excessive OFGs are indeed unfavorable for PDS adsorption. Additionally, the number of electrons (Q) transferred from NC-OH to PDS is 1.011 e,

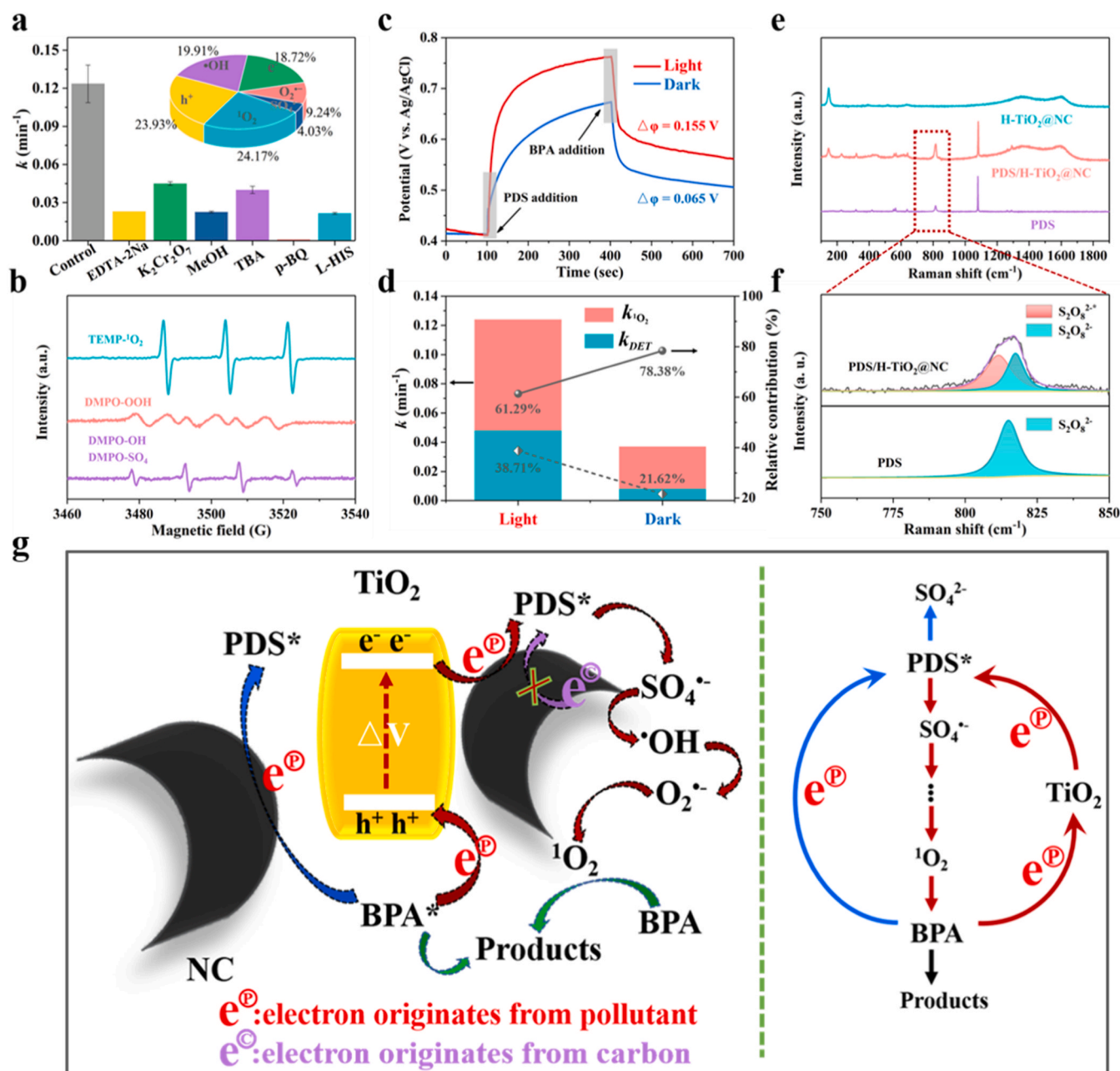


Fig. 6. (a) Quenching experiments of H-TiO₂@NC under light irradiation. (b) EPR spectra. (c) OCP curves. (d) The proportion of $^1\text{O}_2$ and DET. (e and f) In situ Raman spectra. (g) Proposed mechanisms of BPA degradation in H-TiO₂@NC/PDS/light system.

which is significantly higher than that from NC-OH/COOH (0.824 e). It also indicates that PDS is more easily activated on NC-OH. Moreover, compared with NC-OH/COOH, fewer electrons are lost by the carbon atoms of NC-OH. It implies that the oxidation degree of NC-OH is lower than NC-OH/COOH. Based on the PDS activation pathway, the $\text{SO}_4^{\bullet-}$ produced by $\text{S}_2\text{O}_8^{2-}$ can be further transformed into $\text{SO}_4^{\bullet-}$ (Fig. S18). The E_{ads} of $\text{SO}_4^{\bullet-}$ on NC-OH is smaller than NC-OH/COOH, which indicates stronger $\text{SO}_4^{\bullet-}$ adsorption ability on NC-OH. Moreover, the Q of $\text{SO}_4^{\bullet-}$ on NC-OH is higher than NC-OH/COOH (Fig. 5e and h). It suggests that the NC-OH with lower OFGs content is more conducive to $\text{SO}_4^{\bullet-}$ adsorption and the subsequent $\text{SO}_4^{\bullet-}$ generation. Therefore, H-TiO₂@NC with relatively low OFGs content can activate PDS efficiently and keep a remarkable stability.

3.4. Catalytic mechanism

The quenching experiments and EPR tests are employed to investigate the contribution of different active species in the degradation process. Ethylenediaminetetraacetic acid disodium salt (EDTA-2Na) and $\text{K}_2\text{Cr}_2\text{O}_7$ are employed to scavenge h^+ and e^- , respectively. Methanol (MeOH) is an efficient scavenger for $\text{SO}_4^{\bullet-}$ and $\bullet\text{OH}$, while tertiary butyl alcohol (TBA) only quenches $\bullet\text{OH}$ in the solution. In addition, both $\text{O}_2^{\bullet-}$ and $\bullet\text{OH}$ can be scavenged by para-benzoquinone (p-BQ) [45]. $^1\text{O}_2$ can be quenched by L-Histidine (L-HIS). According to the quenching experiments (Fig. S22) and corresponding k values (Table S9), the specific contribution of active species is shown in Fig. 6a. When EDTA-2Na and $\text{K}_2\text{Cr}_2\text{O}_7$ are added into reaction system, the k value decreases to 0.023 and 0.045 min^{-1} , respectively. It implies that h^+ and e^- play an important role for BPA degradation, which also reflects the significance of photoelectron transfer route for PDS activation. The k value decreases from 0.124 to 0.023 min^{-1} after MeOH addition. Moreover, the k value declines to 0.040 min^{-1} with TBA addition, indicating that $\bullet\text{OH}$ shows greater contribution than $\text{SO}_4^{\bullet-}$. Additionally, p-BQ seriously inhibits BPA decomposition with a k value of 0.001 min^{-1} . Compared with $\bullet\text{OH}$, $\text{O}_2^{\bullet-}$ plays a minor role for BPA removal. However, the contribution of $\text{O}_2^{\bullet-}$ is greater than $\text{SO}_4^{\bullet-}$. After L-HIS addition, BPA is greatly suppressed and the corresponding k value decreases to 0.022 min^{-1} , reflecting that $^1\text{O}_2$ plays a crucial role. According to the contribution of active species (inset of Fig. 6a), $^1\text{O}_2$ plays a dominant role for BPA degradation among reactive oxidative species (ROSS). In Fig. S23, the quenching tests of H-TiO₂@NC under dark condition are also explored and the corresponding k values are depicted in Table S10. Similar to the light system, $^1\text{O}_2$ as the main reactive species contribute to BPA degradation under dark condition. It suggests the production pathway of active species cannot be changed by light irradiation. According to the EPR results (Fig. 6b and S24–26), the signal intensities of all the ROSS increase with reaction time. Importantly, the signal of $^1\text{O}_2$ is very weak at 2 min after BPA addition, and the characteristic peaks of $^1\text{O}_2$ disappear with the extension of reaction time (Fig. S26b). It indicates that $^1\text{O}_2$ can be rapidly consumed by BPA, proving $^1\text{O}_2$ primary role for BPA removal.

Carbon-based materials can also activate PDS via DET process. Although $^1\text{O}_2$ plays a dominant role for BPA degradation, ~63% BPA still can be removed within 40 min in this quenching system. Therefore, the DET process is further determined by OCP, EIS and in situ Raman tests. In Fig. 6c, the potential of H-TiO₂@NC electrode increases significantly after PDS addition. During this process, PDS can interact with the H-TiO₂@NC to form complexed PDS, which elevates the potential of the catalyst due to the partial electron transfer from the catalyst to PDS. Subsequently, the potential of electrode drops suddenly when BPA solution is added, indicating that the complexed PDS can abstract electrons from the adsorbed BPA through the conductive carbon framework. Compared with dark system, the potential of complexed PDS is higher and it drops faster under light irradiation ($\Delta\phi = 0.155$ V). According to EIS tests (Fig. S27), light irradiation can decrease the R_{ct} of H-TiO₂@NC greatly from 92.04 Ω to 48.36 Ω . The higher conductivity of H-TiO₂@NC is conducive to the enhancement of DET process. The

contributions of DET process are explored via quenching the $^1\text{O}_2$ generation pathway (Fig. S28). As revealed in Fig. 6d, the k_{DET} in light system is larger than the total k value in dark system. And the contribution of DET process in light system is 38.71%, which is higher than that in dark system (21.62%). It indicates the enhanced DET process with light irradiation, which agrees well with the results of OCP and EIS. Under light irradiation, the photovoltage generated on H-TiO₂@NC can affect the electron distribution of NC layers and improve the conductivity of the catalyst (Fig. S29). Thus, DET process is more likely to occur on H-TiO₂@NC with light irradiation, which is also one of the reasons for the outstanding stability of H-TiO₂@NC. In Fig. 6e and f, in situ Raman tests are further performed to verify DET process. In addition to the characteristic peak of $\text{S}_2\text{O}_8^{2-}$ at ~ 815 cm^{-1} , a new peak ($\text{S}_2\text{O}_8^{\bullet-}$) at ~ 811 cm^{-1} is observed upon the addition of H-TiO₂@NC into PDS solution. This new peak is ascribed to the bending vibrations of the prolonged O-O bond in the metastable H-TiO₂@NC-PDS* complex [28,46]. Therefore, BPA degradation in H-TiO₂@NC/PDS/light system is dominated by non-radical pathways including $^1\text{O}_2$ and DET process.

According to previous reports, $\text{SO}_4^{\bullet-}$ ($E_0(\text{SO}_4^{\bullet-}/\text{SO}_4^{\bullet-}) = 2.5\text{--}3.1$ eV) and $\bullet\text{OH}$ ($E_0(\bullet\text{OH}/\text{H}_2\text{O}) = 1.9\text{--}2.7$ eV) with high redox potentials can effectively degrade various recalcitrant pollutants. However, they can be affected by water quality easily [47,48]. On the contrary, the non-radical pathways including $^1\text{O}_2$, DET, and high-valent metal-oxo species, which almost cannot be influenced by water environment, thus has strong application potential in practical industrial wastewater treatment. In Fig. S30a, the BPA degradation process is slightly affected by anions and natural organic materials (HA). Additionally, the influences of initial pH on BPA degradation are also investigated (Fig. S30b). It can be observed that ~90% of BPA still can be removed within 40 min in a wide pH range (2–11). The degradation performance of H-TiO₂@NC/PDS/light system for other organic contaminants is also studied (Fig. S30c). The pollutants including BPA, SMX and PE both can be degraded rapidly within 40 min. However, CBZ, ATZ and NB contaminants show relatively low removal efficiencies due to the presence of electron-withdrawing groups (-Cl and -NO₂) [38,49]. Therefore, H-TiO₂@NC/PDS/light system is dominated by the non-radical pathway ($^1\text{O}_2$ and DET), which is slightly affected by complicated water matrix and shows great practical application potential.

Combining the above experimental verifications and theoretical calculations, a conceptual model for BPA oxidation in H-TiO₂@NC/PDS/light is proposed (Fig. 6g). The TiO₂ can be excited by light irradiation to separate the electrons and holes. The holes with strong oxidizing ability can abstract the electrons from BPA, which are then transferred rapidly to the surface of NC layers via the electron transport channel. The NC layers with abundant of electrons can activate PDS more easily, which weakens the oxidation of NC layers by PDS. Thus, BPA as an electron source can continuously replenish electrons to TiO₂ to compensate for the depletion of photoelectrons by PDS. After PDS activation, $^1\text{O}_2$ as the dominant ROSS is obtained through a series of successive reactions (Table S11). On the other hand, the enhanced conductivity of H-TiO₂@NC with light irradiation improves the contribution of DET process. During DET process, the electrons supplied by BPA are efficiently transferred to H-TiO₂@NC catalyst and subsequently to PDS, resulting in the reduction of PDS into sulfate ions instead of producing ROSS. Therefore, under light irradiation, the electron transfer route tuning for PDS activation and DET process enhancement both contribute to the stability improvement of H-TiO₂@NC.

4. Conclusions

In this work, a hollow structure with TiO₂ nanoparticles supported on the inner surface of N-doped carbon spheres (H-TiO₂@NC) is synthesized via CVD process, which is an effective catalyst for Fenton-like reactions under light irradiation. Compared to H-TiO₂@NC/PDS/dark system, H-TiO₂@NC/PDS/light system displays excellent stability for BPA degradation. According to experiments and theoretical

calculations, C-OH and COOH groups increasement is the main reason for the deactivation of H-TiO₂ @NC catalyst. Importantly, the increase rate of C-OH and COOH groups under light irradiation is much slower than that dark condition. The photoelectron transfer route weakens the supply of electrons to PDS from the carbon atoms around graphitic N, which tremendously reduces the oxidation of carbon framework. Additionally, DET process is improved due to conductivity enhancement under light irradiation, which also weakens the oxidation of carbon skeleton. Therefore, the stability of H-TiO₂ @NC catalyst is greatly improved due to electron transfer route tuning and DET process enhancement. The findings in this study give some new insights into the deactivation mechanism of N-doped carbon materials during PDS-based AOPs. Impressively, this work provides a reliable strategy for improving the stability of N-doped carbon materials through the ingenious introduction and construction of photocatalysts. This concept is expected to be extended to the construction of carbon-based materials with other photocatalysts.

Supporting information

Additional details on the reagents, analytical data, calculation methods, and other associated supplementary texts, tables, and figures.

CRediT authorship contribution statement

Liu Xiaomei: Conceptualization, Methodology, Investigation, Writing – original draft. **Wang Jun:** Formal analysis, Visualization. **Liao Tao:** Validation, Software. **Li Yang:** Writing – review & editing. **Fan Xiaobin:** Writing – review & editing. **Zhang Fengbao:** Writing – review & editing. **Peng Wenchao:** Resources, Conceptualization, Writing – review & editing, Supervision, Data curation.

Declaration of Competing Interest

The authors declare that they have no known competing financial interests or personal relationships that could have appeared to influence the work reported in this paper.

Data availability

Data will be made available on request.

Acknowledgements

This research was supported by No. U20A20153 from the National Natural Science Foundation of China.

Appendix A. Supporting information

Supplementary data associated with this article can be found in the online version at [doi:10.1016/j.apcatb.2023.123261](https://doi.org/10.1016/j.apcatb.2023.123261).

References

- G.L. Wang, S. Chen, X. Quan, H.T. Yu, Y.B. Zhang, Enhanced activation of peroxymonosulfate by nitrogen doped porous carbon for effective removal of organic pollutants, *Carbon* 115 (2017) 730–739.
- W. Ren, G. Nie, P. Zhou, H. Zhang, X.G. Duan, S.B. Wang, The intrinsic nature of persulfate activation and N-doping in carbocatalysis, *Environ. Sci. Technol.* 54 (2020) 6438–6447.
- Y.W. Gao, Z.H. Chen, Y. Zhu, T. Li, C. Hu, New Insights into the generation of singlet oxygen in the metal free peroxymonosulfate activation process: important role of electron-deficient carbon atoms, *Environ. Sci. Technol.* 54 (2020) 1232–1241.
- J. Wang, X.G. Duan, J. Gao, Y. Shen, X.H. Feng, Z.J. Yu, X.Y. Tan, S.M. Liu, S. B. Wang, Roles of structure defect, oxygen groups and heteroatom doping on carbon in nonradical oxidation of water contaminants, *Water Res* 185 (2020), 116244 (No.).
- X.G. Duan, H.Q. Sun, Y.X. Wang, J. Kang, S.B. Wang, N-doping induced nonradical reaction on single-walled carbon nanotubes for catalytic phenol oxidation, *ACS Catal.* 5 (2015) 553–559.
- D.G. Li, X.G. Duan, H.Q. Sun, J. Kang, H.Y. Zhang, M.O. Tade, S.B. Wang, Facile synthesis of nitrogen-doped graphene via low-temperature pyrolysis: the effects of precursors and annealing ambience on metal-free catalytic oxidation, *Carbon* 115 (2017) 649–658.
- X.T. Li, J. Wang, X.G. Duan, Y. Li, X.B. Fan, G.L. Zhang, F.B. Zhang, W.C. Peng, Fine-Tuning Radical/Nonradical Pathways on Graphene by Porous Engineering and Doping Strategies, *ACS Catal.* 11 (2021) 4848–4861.
- W. Zhang, Y. Li, X.B. Fan, F.B. Zhang, G.L. Zhang, Y.A. Zhu, W.C. Peng, S.B. Wang, X.G. Duan, Synergy of nitrogen doping and structural defects on hierarchically porous carbons toward catalytic oxidation via a non-radical pathway, *Carbon* 155 (2019) 268–278.
- B. Ma, B. Li, Y. Li, X.B. Fan, F.B. Zhang, G.L. Zhang, Y.Z. Zhu, W.C. Peng, Synthesis of nitrogen and sulfur Co-doped carbon with special hollow sphere structure for enhanced catalytic oxidation, *Sep. Purif. Technol.* 278 (2022), 119522 (No.).
- Z. Yang, X.G. Duan, J. Wang, Y. Li, X.B. Fan, F.B. Zhang, G.L. Zhang, W.C. Peng, Facile synthesis of high-performance nitrogen-doped hierarchically porous carbon for catalytic oxidation, *ACS Sustain. Chem. Eng.* 8 (2020) 4236–4243.
- Y. Wang, Z.P. Zhang, Z.L. Yin, Z.F. Liu, Y.L. Liu, Z. Yang, W.B. Yang, Adsorption and catalysis of peroxymonosulfate on carbocatalysts for phenol degradation: The role of pyrrolic-nitrogen, *Appl. Catal. B Environ.* 319 (2022), 121891 (No.).
- P.D. Hu, H.R. Su, Z.Y. Chen, C.Y. Yu, Q.L. Li, B.X. Zhou, P.J.J. Alvarez, M.C. Long, Selective degradation of organic pollutants using an efficient metal-free catalyst derived from carbonized polypyrrole via peroxymonosulfate activation, *Environ. Sci. Technol.* 51 (2017) 11288–11296.
- Q. Wang, X.M. Liu, A. Cai, H.W. He, G.L. Zhang, F.B. Zhang, X.B. Fan, W.C. Peng, Y. Li, Atomically Fe doped hollow mesoporous carbon spheres for peroxymonosulfate mediated advanced oxidation processes with a dual activation pathway, *J. Mater. Chem. A* 10 (2022) 20535–20544.
- W. Ren, L.L. Xiong, G. Nie, H. Zhang, X.G. Duan, S.B. Wang, Insights into the electron-transfer regime of peroxydisulfate activation on carbon nanotubes: the role of oxygen functional groups, *Environ. Sci. Technol.* 54 (2020) 1267–1275.
- Q.Q. Jia, Y. Gao, Y. Li, X.B. Fan, F.B. Zhang, G.L. Zhang, W.C. Peng, S.B. Wang, Cobalt nanoparticles embedded in N-doped carbon on carbon cloth as free-standing electrodes for electrochemically-assisted catalytic oxidation of phenol and overall water splitting, *Carbon* 155 (2019) 287–297.
- X.M. Liu, Y. Li, X.B. Fan, F.B. Zhang, G.L. Zhang, W.C. Peng, Photo-accelerated Co³⁺/Co²⁺ transformation on cobalt and phosphorus co-doped g-C₃N₄ for Fenton-like reaction, *J. Mater. Chem. A* 9 (2021) 22399–22409.
- A.Q. Wang, Y.W. Chen, Z.K. Zheng, H. Wang, X. Li, Z.Y. Yang, R.L. Qiu, K. Yan, In situ N-doped carbon-coated mulberry-like cobalt manganese oxide boosting for visible light driving photocatalytic degradation of pharmaceutical pollutants, *Chem. Eng. J.* 411 (2021), 128497 (No.).
- Y. Li, B. Yu, B. Liu, X. Yu, G. Qin, M.H. Fan, Y.C. Zhang, L.L. Wang, Superior Fenton-like and photo-Fenton-like activity of MoS₂@TiO₂/N-doped carbon nanofibers with phase-regulated and vertically grown MoS₂ nanosheets, *Chem. Eng. J.* 452 (2023), 139542 (No.).
- M.M. Mian, G.J. Liu, B. Yousaf, B. Fu, R. Ahmed, Q. Abbas, M.A.M. Munir, L. Ruijia, One-step synthesis of N-doped metal/biochar composite using NH₃-ambience pyrolysis for efficient degradation and mineralization of Methylene Blue, *J. Environ. Sci.* 78 (2019) 29–41.
- A.H. Asif, N. Rafique, R.A.K. Hirani, L. Shi, S. Zhang, S.B. Wang, H.Q. Sun, Graphitic carbon nitride engineered α-Fe₂O₃/rGO heterostructure for visible-light-driven photochemical oxidation of sulfamethoxazole, *Chem. Eng. J.* 451 (2023), 138630 (No.).
- W. Ren, C. Cheng, P.H. Shao, X.B. Luo, H. Zhang, S.B. Wang, X.G. Duan, Origins of Electron-Transfer Regime in Persulfate-Based Nonradical Oxidation Processes, *Environ. Sci. Technol.* 56 (2022) 78–97.
- J. Miao, W. Geng, P.J.J. Alvarez, M.C. Long, 2D N-doped porous carbon derived from polydopamine-coated graphitic carbon nitride for efficient non-radical activation of peroxymonosulfate, *Environ. Sci. Technol.* 54 (2020) 8473–8481.
- W. Ren, Q.M. Zhang, C. Cheng, F. Miao, H. Zhang, X.B. Luo, S.B. Wang, X.G. Duan, Electro-induced carbon nanotube discrete electrodes for sustainable persulfate activation, *Environ. Sci. Technol.* 56 (2022) 14019–14029.
- C.X. Zhang, C.F. Xie, Y.Y. Gao, X.P. Tao, C.M. Ding, F.T. Fan, H.L. Jiang, Charge separation by creating band bending in metal-organic frameworks for improved photocatalytic hydrogen evolution, *Angew. Chem. Int. Ed.* 61 (2022), 202204 (No.).
- R.T. Chen, Z.F. Ren, Y. Liang, G.H. Zhang, T. Dittrich, R.Z. Liu, Y. Liu, Y. Zhao, S. Pang, H.Y. An, C.W. Ni, P.W. Zhou, K.L. Han, F.T. Fan, C. Li, Spatiotemporal imaging of charge transfer in photocatalyst particles, *Nature* 610 (2022) 296–301.
- J.J. Sun, X.Y. Li, Q.D. Zhao, B.J. Liu, Ultrathin nanoflake-assembled hierarchical BiOBr microflower with highly exposed {001} facets for efficient photocatalytic degradation of gaseous ortho-dichlorobenzene, *Appl. Catal. B: Environ.* 281 (2021), 119478 (No.).
- S. Son, S.H. Hwang, C. Kim, J.Y. Yun, J. Jang, Designed synthesis of SiO₂/TiO₂ core/shell structure as light scattering material for highly efficient dyesensitized solar cells, *ACS Appl. Mater. Interfaces* 5 (2013) 4815–4820.
- X.M. Liu, J. Wang, D. Wu, Z. Wang, Y. Li, X.B. Fan, F.B. Zhang, G.L. Zhang, W. C. Peng, N-doped carbon dots decorated 3D g-C₃N₄ for visible-light driven peroxydisulfate activation: Insights of non-radical route induced by Na⁺ doping, *Appl. Catal. B: Environ.* 310 (2022), 121304 (No.).

- [29] F.L. Wang, T.T. Hou, X. Zhao, W. Yao, R.Q. Fang, K. Shen, Y.W. Li, Ordered macroporous carbonous frameworks implanted with CdS quantum dots for efficient photocatalytic CO₂ reduction, *Adv. Mater.* 33 (2021) 2102690.
- [30] X.W. Ruan, X.Q. Cui, Y. Cui, X.F. Fan, Z.Y. Li, T.F. Xie, K.K. Ba, G.R. Jia, H. Y. Zhang, L. Zhang, W. Zhang, X. Zhao, J. Leng, S.Y. Jin, D.J. Singh, W.T. Zheng, Favorable Energy Band Alignment of TiO₂ Anatase/Rutile Heterophase Homojunctions Yields Photocatalytic Hydrogen Evolution with Quantum Efficiency Exceeding 45.6%, *Adv. Energy Mater.* 12 (2022) 2200298 (No.).
- [31] L.K. Preethi, T. Mathews, M. Nand, S.N. Jha, C.S. Gopinath, S. Dash, Band alignment and charge transfer pathway in three phase anatase-rutile-brookite TiO₂ nanotubes: An efficient photocatalyst for water splitting, *Appl. Catal. B: Environ.* 6 (2017) 9–19.
- [32] J. Yin, W.L. Zhang, N.A. Alhebshi, N. Salah, H.N. Alshareef, Synthesis strategies of porous carbon for supercapacitor applications, *Small Methods* 4 (2020) 1900853 (No.).
- [33] R.A. Spurr, H. Myers, Quantitative analysis of anatase-rutile mixtures with an X-ray diffractometer, *Anal. Chem.* 29 (1957) 760–762.
- [34] Q. Cheng, Y.J. Yuan, R. Tang, Q.Y. Liu, L. Bao, P. Wang, J.S. Zhong, Z.Y. Zhao, Z. T. Yu, Z.G. Zou, Rapid hydroxyl radical generation on (001)-Facet-exposed ultrathin anatase TiO₂ nanosheets for enhanced photocatalytic lignocellulose-to-H₂ conversion, *ACS Catal.* 12 (2022) 2118–2125.
- [35] X.H. Wang, Z.K. Xiong, H.L. Shi, Z.L. Wu, B.K. Huang, H. Zhang, P. Zhou, Z.C. Pan, W. Liu, B. Lai, Switching the reaction mechanisms and pollutant degradation routes through active center size-dependent Fenton-like catalysis, *Appl. Catal. B: Environ.* 329 (2023), 122569 (No.).
- [36] L.P. Wu, B. Li, Y. Li, X.B. Fan, F.B. Zhang, G.L. Zhang, Q. Xia, W.C. Peng, Preferential Growth of the Cobalt (200) Facet in Co@N-C for Enhanced Performance in a Fenton-like Reaction, *ACS Catal.* 11 (2021) 5532–5543.
- [37] X.G. Duan, H.Q. Sun, Z.M. Ao, L. Zhou, G.X. Wang, S.B. Wang, Unveiling the active sites of graphene catalyzed peroxymonosulfate activation, *Carbon* 107 (2016) 371–378.
- [38] B. Li, B. Ma, M.Y. Wei, Y. Li, X.B. Fan, F.B. Zhang, G.L. Zhang, Q. Xia, W.C. Peng, Synthesis of Co-NC catalysts from spent lithium-ion batteries for fenton-like reaction: Generation of singlet oxygen with ~100% selectivity, *Carbon* 197 (2022) 76–86.
- [39] D.S. Bergsman, B.A. Getachew, C.B. Cooper, J.C. Grossman, Preserving nanoscale features in polymers during laser induced graphene formation using sequential infiltration synthesis, *Nat. Commun.* 11 (2020) 3636 (No.).
- [40] H. Li, Z.B. Xia, J.Q. Chen, L. Lei, J.H. Xing, Constructing ternary CdS/reduced graphene oxide/TiO₂ nanotube arrays hybrids for enhanced visible-light-driven photoelectrochemical and photocatalytic activity, *Appl. Catal. B: Environ.* 168 (2015) 105–113.
- [41] B.J. Ng, L.K. Putri, L.L. Tan, P. Pasbakhsh, S.P. Chai, All-solid-state Z-scheme photocatalyst with carbon nanotubes as an electron mediator for hydrogen evolution under simulated solar light, *Chem. Eng. J.* 316 (2017) 41–49.
- [42] W.W. Han, L.L. Chen, W.Y. Song, S.B. Wang, X.B. Fan, Y. Li, F.B. Zhang, G. L. Zhang, W.C. Peng, Synthesis of nitrogen and sulfur co-doped reduced graphene oxide as efficient metal-free cocatalyst for the photo-activity enhancement of CdS, *Appl. Catal. B: Environ.* 236 (2018) 212–221.
- [43] L. Tang, Y.N. Liu, J.J. Wang, G.M. Zeng, Y.C. Deng, H.R. Dong, H.P. Feng, J. J. Wang, B. Peng, Enhanced activation process of persulfate by mesoporous carbon for degradation of aqueous organic pollutants: Electron transfer mechanism, *Appl. Catal. B: Environ.* 231 (2018) 1–10.
- [44] C.B. Bie, B.C. Zhu, F.Y. Xu, L.Y. Zhang, J.G. Yu, In Situ Grown Monolayer N-Doped Graphene on CdS Hollow Spheres with Seamless Contact for Photocatalytic CO₂ Reduction, *Adv. Mater.* 31 (2019) 1902868 (No.).
- [45] J.P. Liang, L. Fu, K. Gao, X.G. Duan, Accelerating radical generation from peroxymonosulfate by confined variable co species toward ciprofloxacin mineralization: ROS quantification and mechanisms elucidation, *Appl. Catal. B: Environ.* 315 (2022), 121542 (No.).
- [46] W. Ren, L.L. Xiong, X.H. Yuan, Z.W. Yu, H. Zhang, X.G. Duan, S.B. Wang, Activation of peroxydisulfate on carbon nanotubes: electron-transfer mechanism, *Environ. Sci. Technol.* 53 (2019) 14595–14603.
- [47] S.X. Wang, J.Y. Tian, Q. Wang, F. Xia, S.S. Gao, W.X. Shi, F.Y. Cui, Development of CuO coated ceramic hollow fiber membrane for peroxymonosulfate activation: a highly efficient singlet oxygen-dominated oxidation process for bisphenol a degradation, *Appl. Catal. B: Environ.* 256 (2019), 117783 (No.).
- [48] L.L. Xiong, W. Ren, H. Lin, H. Zhang, Efficient removal of bisphenol A with activation of peroxydisulfate via electrochemically assisted Fe(III)-nitrilotriacetic acid system under neutral condition, *J. Hazard. Mater.* 403 (2021), 123874 (No.).
- [49] S. Liu, C. Zhao, Z.Y. Wang, H.J. Ding, H.P. Deng, G. Yang, J.F. Li, H.L. Zheng, Urea-assisted one-step fabrication of a novel nitrogen-doped carbon fiber aerogel from cotton as metal-free catalyst in peroxymonosulfate activation for efficient degradation of carbamazepine, *Chem. Eng. J.* 386 (2020), 124015 (No.).